BIOMATERIALS

Does the mantis shrimp pack a phononic shield?

N. A. Alderete[1], S. Sandeep[2], S. Raetz[2], M. Asgari[1]†, M. Abi Ghanem[3]*, H. D. Espinosa[1]*

The powerful strikes generated by the smasher mantis shrimp require it to possess a robust protection mechanism to withstand the resultant forces. Although recent studies have suggested that phononic bandgaps complement the mantis shrimp's defensive suite, direct experimental evidence for this mechanism has remained elusive. In this work, we explored the phononic properties of the mantis shrimp's dactyl club using laser ultrasonic techniques and numerical simulations. Our results demonstrate that the dactyl club's periodic region functions as a dispersive, high-quality graded system, exhibiting Bloch harmonics, flat dispersion branches, ultraslow wave modes, and wide Bragg bandgaps in the lower megahertz range. These features effectively shield the shrimp from harmful high-frequency stress waves generated by cavitation bubble collapse events during impact.

Among the various notable evolutionary adaptations displayed by the animal kingdom (*1*–*6*) lies the ability to withstand high peak forces delivered over short periods of time (*7*). Perhaps the most formidable species that exhibits this capability is the renowned peacock mantis shrimp (*Odontodactylus scyllarus*), a smasher stomatopod native to the Indo-Pacific seabed (Fig. 1A). Despite its relatively small size (ranging from 3 to 18 cm), this mantis shrimp is known to execute a well-orchestrated strike sequence that spans over seven orders of magnitude in time (from hundreds of milliseconds to nanoseconds) (*8*) and reaches peak forces in the vicinity of ~1500 N (i.e., exceeding 1000 times its body weight) (*9*). At the center of this distinctive attack system is the mantis shrimp's dactyl club (Fig. 1B), a hammer-shaped appendage that impacts the target in less than 50 μs (*9*) and generates cavitation bubbles that, upon collapse (*8*, *10*), trigger ultrashort nanosecond shock waves with frequency contents that can reach hundreds of MHz (*11*, *12*). As such, each strike delivers a dual blow capable of breaking hard exoskeletons. Unlike other natural attack systems, which are used only once (*13*), the dactyl club can strike multiple times in between molting cycles without sustaining macroscopic fracture.

A major contributing element to the dactyl club's strike power is its hierarchical design, made from a limited but exquisitely tuned arrangement of mineral and organic materials (*14*). Three distinct layers make up the club from the exterior to the interior: the impact surface, the impact region, and the periodic region (Fig. 1C). The impact surface is a hard (~60 GPa), thin (~70 μm) hydroxyapatite coating that prevents catastrophic failure by exhibiting viscoplasticity and localized damage (*15*). Next, the impact region (~500 μm) consists of mineralized chitin fibers in a herringbone architecture, which enable damage dissipation through diffuse cracking, crack arrest, and crack deflection (*14*, *16*). Last, the periodic region features a spatially graded Bouligand arrangement of chitin fiber bundles [~80- to 10-μm pitch (p), 2° to 6° interlayer rotation angle (ψ)] (*17*), which modulates stress wave propagation during impact, akin to a backing layer. Together, these region-specific mechanisms form a synergistic protection system that withstands repeated high-intensity impacts without substantial damage.

It has been proposed that the Bouligand structure also endows the dactyl club with shear wave–filtering capabilities in the form of ultrasonic phononic bandgaps (i.e., select frequency ranges at which the propagation of elastic energy is forbidden or strongly attenuated) (*18*). Although phononic bandgaps have been put forward as an optimized engineering strategy for prey-predator interactions (*19*), experimental evidence of phononic behavior in nature remains rare, particularly when compared with the more extensively documented biophotonic phenomena (*20*). Notably, experiments have shown that the scales covering the wings of certain moth species have evolved to absorb sound waves, through local resonance in the 20- to 160-kHz range, and provide acoustic camouflage against the echolocating sonar of predatory bats (*21*).

Motivated by the limited understanding of the phononics of the dactyl club, we investigated the dispersion characteristics of the impact and periodic regions across various acoustic scales by using two optoacoustic setups and finite element analysis (FEA). Specifically, we analyzed surface acoustic wave (SAW) propagation in the MHz range within these regions using nanosecond and picosecond pump-probe laser ultrasonics (NLU and PLU, respectively) setups. Laser ultrasonics techniques were chosen for their ability to generate nondestructive ultrasonic and hypersonic waves and for their capacity to spatially interrogate the sample. The use of SAWs, which combine longitudinally and transversely polarized waves (with a predominant detection of the latter due to the technique's sensitivity to out-of-plane motion), was particularly suited for this study. This approach was grounded on the established notion that helicoidal fiber arrangements primarily influence shear wave propagation while leaving longitudinal waves mostly unaffected (*22*). Additionally, studying wave propagation on the surface of the dactyl club provided access to distinct local regions, offering a spatially targeted view of wave phenomena on the club. Selection of the temporal regime responds to the characteristic length scales of the periodic region and to the fact that shrimp impacts contain frequencies in the ultrasonic range (*9*), which has led to shrimp-inspired solutions that point to ultrasonic filtering as a key attenuation mechanism (*23*). Furthermore, combined access to nanosecond and picosecond scales provides insight into the hierarchy of the periodic region, from the effective medium scale down to the individual layers that make up the Bouligand structure. As such, and in line with the hypothesis of the dactyl club's phononic capabilities, our experimental measurements and computational analyses unveiled a complex phononic landscape, with dispersion effects stemming from a variety of mechanisms elicited by the multiscale, hierarchical nature of the dactyl club.

Results

NLU experiments

The phononic spectra of the dactyl club's impact and periodic regions were first investigated using a time-resolved pump-probe NLU method called transient grating spectroscopy (TGS; Fig. 1D). In TGS, two subnanosecond laser pump pulses are crossed at an angle at the aluminum-coated surface of the sample, forming an optical interference pattern (*24*). The elicited rapid thermoelastic expansion in the metal generates counterpropagating SAWs with an acoustic wavelength (λ_{ac}) equal to the spacing of the optical interference fringes. In the experiment, SAWs were monitored in the time domain by measuring the diffraction of a quasi–continuous wave probe beam caused by the transient vertical displacement of the surface (see materials and methods section S3). SAW-modes propagating in the xz plane (i.e., across or along the Bouligand layers) result in high-frequency oscillations in the signal. By varying the acoustic wavelength (Fig. 1D) and analyzing the spectrum of each measured signal, the frequency–acoustic wave number (f-k) relationship can be established, enabling characterization of the material's phononic dispersion.

[1]Department of Mechanical Engineering, Northwestern University, Evanston, IL, USA. [2]Laboratoire d'Acoustique de l'Université du Mans (LAUM), UMR 6613, Institut d'Acoustique–Graduate School (IA–GS), CNRS, Le Mans Université, Le Mans, France. [3]Universite Claude Bernard Lyon 1, CNRS, Institut Lumière Matière, Villeurbanne, France.
*Corresponding author. Email: maroun.abi-ghanem@univ-lyon1.fr (M.A.G.); espinosa@northwestern.edu (H.D.E.)
†Present address: Department of Medical Engineering, University of South Florida, Tampa, FL, USA.

Downloaded from https://www.science.org at Zhejiang University on September 10, 2025

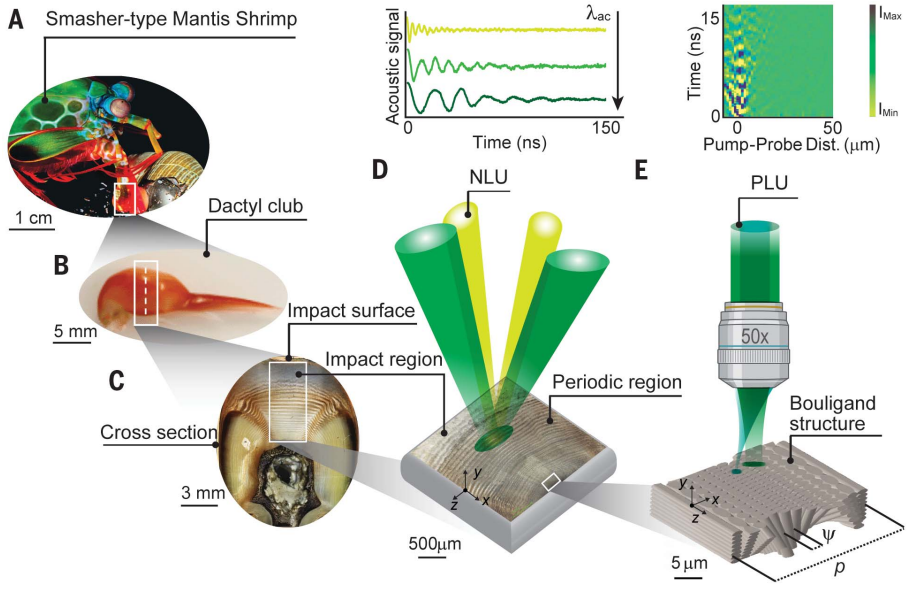

Fig. 1. Mantis shrimp club and our approach to characterize its phononic behavior. (**A**) Smasher mantis shrimp using its dactyl club against a seashell. [Photo credit: R. Caldwell] (**B**) Dissected dactyl club (whole, side view). (**C**) Transverse cross section of the club with distinct layers highlighted. (**D** and **E**) Schematic and characteristic signals of (D) NLU characterization of the impact and periodic regions by TGS and (E) PLU characterization by ASOPS, as well as a schematic of the Bouligand arrangement of the fibers with a relative angle between plies (ψ) and pitch (p).

The TGS technique provides access to surface acoustic phonons with wavelengths ranging from 6 to 31 μm.

To gain insight into the mechanical properties of the club, we measured the frequency variation of SAWs along the z direction at a fixed acoustic wavelength (λ_{ac} = 30 μm). We examined four different spots: one in the impact region (~200 μm from the impact–periodic region interface; blue spot in Fig. 2B) and three within the periodic region with characteristic pitches of p = 45, 40, and 35 μm (green, blue, and orange spots in Fig. 2B). We note that the pitch within the periodic region varies continuously in a gradient fashion and that the reported pitch values represent an average periodicity measured over the probed spot size. From measured frequencies, the variation in phase velocity of the SAWs was obtained from $v_{SAW}^{LW} = f_{SAW}\lambda_{ac}$, where LW is long wavelength, as shown in Fig. 2A. A clear change in phase velocity was identified from faster to slower speeds. These results are consistent with previously reported elastic modulus measurements of 30 to 60 GPa in the impact region and a lower modulus, ranging from ~10 to 20 GPa, in the periodic region (*14*).

Next, we performed TGS experiments to obtain dispersion curves for acoustic waves propagating along the x direction of the sample (Fig. 2C). The impact region exhibited a dispersionless curve with a single SAW mode at a phase velocity of 2380 m s^{-1}. By contrast, the periodic region displayed a more complex behavior, featuring two primary propagating SAW modes with average phase velocities of 3450 and 1540 m s^{-1}, corresponding to surface skimming longitudinal (SSL) and Rayleigh (R) waves, respectively. These velocities align well with longitudinal and transverse wave speeds estimated from composite properties by static indentation tests (*14*, *18*). The invariance of R- and SSL-wave velocities with respect to pitch is consistent with the presence of a composite made of transverse isotropic laminas with similar mechanical properties and stacking characteristics. Additionally, for pitches of p = 45 and 40 μm, another propagating mode with a phase velocity of 2030 m s^{-1} (SAW-2) branches from the R-wave mode around k = 0.3 μm^{-1}.

In addition to the aforementioned modes, we observe a mode parallel to the R-mode that was characterized by a similar group velocity ($v_g = d\omega/dk$, where ω is the angular frequency) but shifted by a spacing (Δk). This shift is evident in all three dispersion diagrams of the periodic region (green, purple, and orange diagrams) but absent in the impact region (blue diagram) (Fig. 2C). Notably, this spacing, indicated by double-headed arrows in the diagrams, increases as the pitch decreases. Between the identified modes (dotted lines), several additional frequency peaks are detected, which appear to correspond to small segments of other acoustic modes (see, for example, the black and orange arrows in Figs. 2C and 3B, respectively, and spectrograms in supplementary text section S1). Additionally, low-frequency oscillatory signals (<50 MHz, mode A along dashed lines) are present in all dispersion diagrams, consistent with acoustic oscillations in air (*25*).

To interpret TGS experimental observations, we used finite element modeling (FEM) to simulate SAW propagation through idealized periodic microstructures with geometric pitches matching those in the experiments. Because the wavelengths probed by TGS are much larger than the fiber diameter and interfiber distance, we modeled the Bouligand microstructure as a composite laminate of transversely isotropic laminas. For the composite's physical and mechanical properties, we adopted values reported by Guarín-Zapata *et al.* (*18*), that is, ρ = 1400 kg m^{-3}, E_T = 30 GPa, E_P = 15 GPa, G_{TP} = 1.65 GPa, and $v_P = v_{TP}$ = 0.25, where ρ, E, and G are the density, elastic modulus, and shear modulus, respectively, and subscripts T and P refer to transverse and plane properties, respectively. The components of the stiffness matrix (C_{ij}), as a function of the ply rotation angle, are shown in the polar plots of Fig. 3A. We assumed an interply rotation angle of ψ = 5°, which resulted in ply thicknesses ($t = p\psi/180°$) on the order of ~1 μm, consistent with previous reports (*17*).

Figure 3B presents the FEM-obtained dispersion diagrams for p = 45, 40, and 35 μm alongside the experimental data. The computational results reveal a complex dispersion landscape with several key features. First, a repetitive pattern emerges, marked by parallel propagative lines above 25 MHz and characteristic branch folding (peaks and valleys) below 25 MHz. This pattern results from considering wave numbers that span multiple Brillouin zones (BZs), where the BZ length is $\mathrm{BZ}\left[-\frac{\pi}{p}, \frac{\pi}{p}\right]$. As the pitch decreases, the number of repeated patterns decreases within the same wave number range. This periodic repetition of the pattern at exact integer multiples of the BZ gives rise to Bloch harmonic modes, highlighted for the SSL- and R-modes by white dashed lines. For instance, at p = 45 μm, ~6 Bloch harmonics fit within the wave number range 0 to 1 μm^{-1}, whereas at p = 35 μm, ~5 Bloch harmonics fit within the same range. These Bloch harmonic lines appear parallel because they share the same group velocity and correspond to the same acoustic mode. As the pitch decreases, the spacing between these Bloch harmonics (Δk) increases. To focus on the most relevant features, we examined the first two BZs for p = 45 μm, as shown in the expanded view of Fig. 3B. The diagram reveals the nondispersive nature of the SSL-mode and the opening of a bandgap (indicated by dotted lines and BG) for the R-wave mode around 25 MHz, with a width of ~2 MHz. The different dispersion characteristics of these modes can be attributed to the modulation of the relevant elastic

Downloaded from https://www.science.org at Zhejiang University on September 10, 2025

constants along the pitch: The SSL-mode, with its main displacement along the x axis, experiences no elastic modulation, whereas the R-wave, with its displacement along the y axis, is modulated elastically. The R-wave bandgap, predicted for all pitches (p = 45, 40, and 35 μm), widens as the pitch decreases.

By comparing the numerically obtained dispersion diagrams with the experimental data, we identified three key findings. First, the model-predicted phase velocities align well with the experimentally measured phase velocities of the R-wave and SSL-waves, validating both the model and the used mechanical properties. Second, consistent with simulations, R-wave

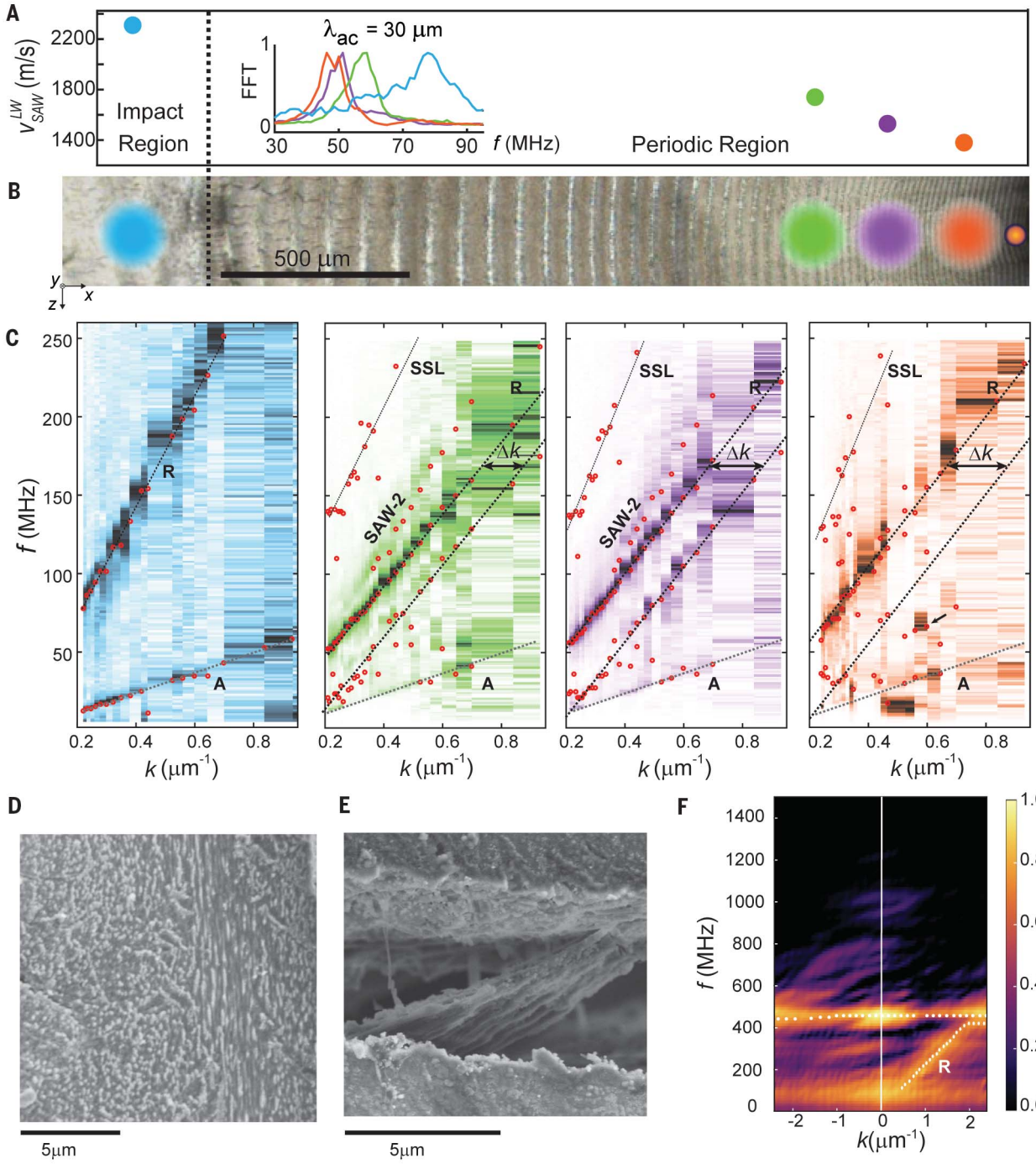

Fig. 2. Ultrasonic phononic dispersion of the mantis shrimp's dactyl club. (**A**) Frequency (f) spectrogram obtained by fast Fourier transform (FFT) and phase speed variation in the impact and periodic regions obtained by TGS at an acoustic wavelength (λ_{ac} = 30 μm). (**B**) Enlarged view of the cross section of the dactyl club with regions probed by TGS (large spot sizes) and PLU (small spot size); the colored regions illustrate the position and sizes of the probed regions. (**C**) Phononic dispersion curves obtained from TGS at locations highlighted in (B). (**D** and **E**) SEM images of the region probed by PLU showing (D) the chitinous-organic composite and (E) fiber bundles made of individual chitin fibrils. (**F**) Phononic dispersion curves obtained from PLU. Red and white dots in (C) and (F), respectively, represent pixels with maximum intensity in the pseudocolor plots.

Downloaded from https://www.science.org at Zhejiang University on September 10, 2025

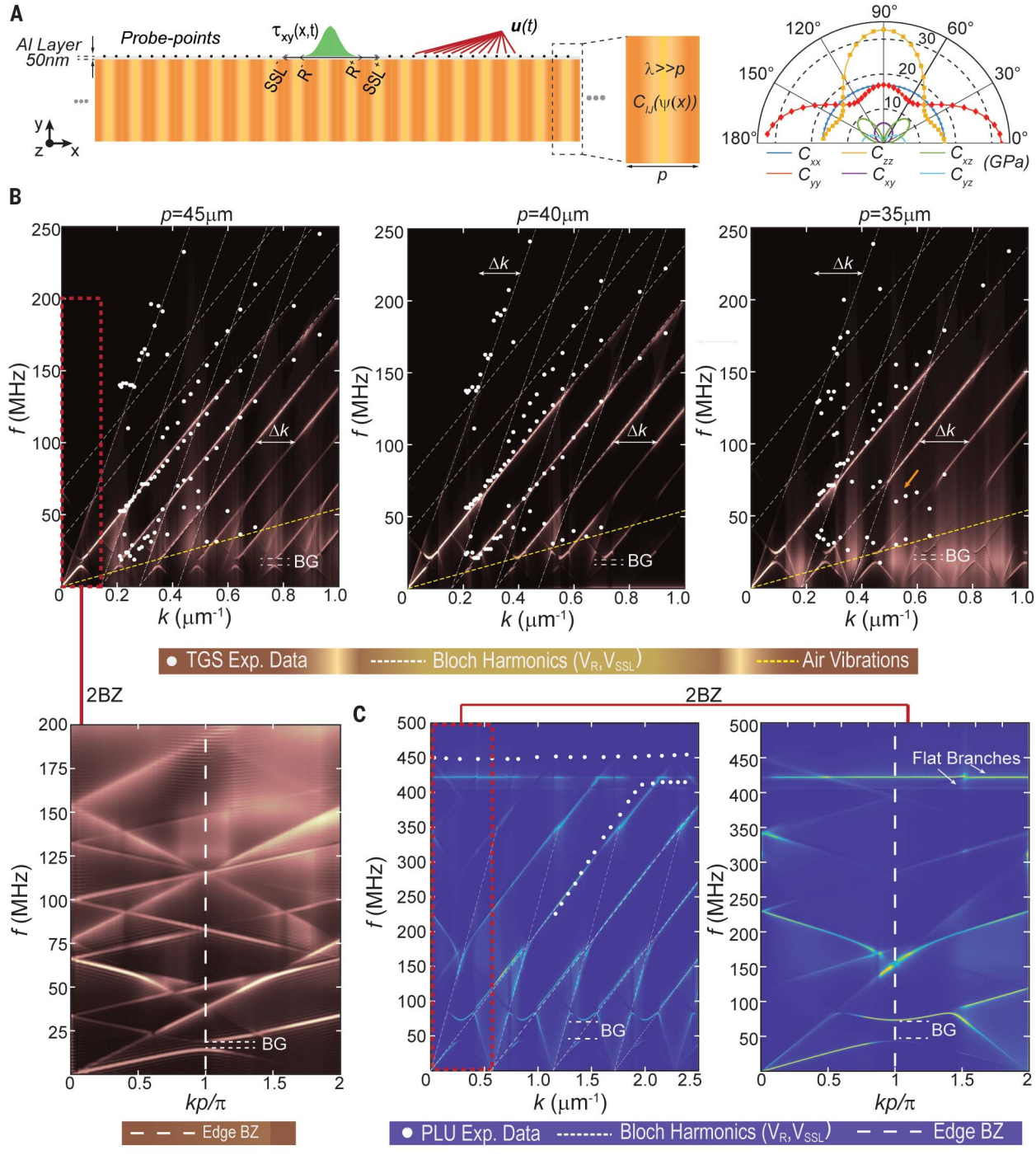

Fig. 3. Finite element simulations of phononic dispersion. (**A**) Schematic of simulation domain for surface wave propagation in the Bouligand microstructure. Applied surface traction τ_{xy} (x, t), displacement field $u(t)$ collection points (where u is displacement), and angular variation of the stiffness matrix components are shown. (**B**) FEM-obtained surface wave dispersion diagrams (k-f) for three pitches. Experimental points obtained with TGS are superimposed. For the case p = 45 μm, a detailed view of the first two BZs is shown (the edge of the first BZ is shown as a dashed line). In all cases, the bandgap for R-waves is highlighted. (**C**) FEM-obtained surface wave dispersion diagrams (k-f), with experimental points superimposed for the region probed by PLU. A zoomed-in view within the first two BZs is also depicted.

Bloch harmonic modes (parallel modes shifted by Δk in Fig. 2C) are detected experimentally, whereas SSL-wave Bloch harmonics are less pronounced, likely because of the technique's sensitivity to y-axis displacement. Some peaks labeled as SAW-2 in Fig. 2C may correspond to SSL-wave Bloch harmonics crossing R-wave Bloch harmonics, or they could indicate a second pseudosurface acoustic mode, which is commonly seen in waves propagating on anisotropic surfaces (*26*). This second mode warrants further investigation beyond the scope of this study (see additional details in supplementary text section S3). Third, the observed increase in Δk with decreasing pitch confirms

Downloaded from https://www.science.org at Zhejiang University on September 10, 2025

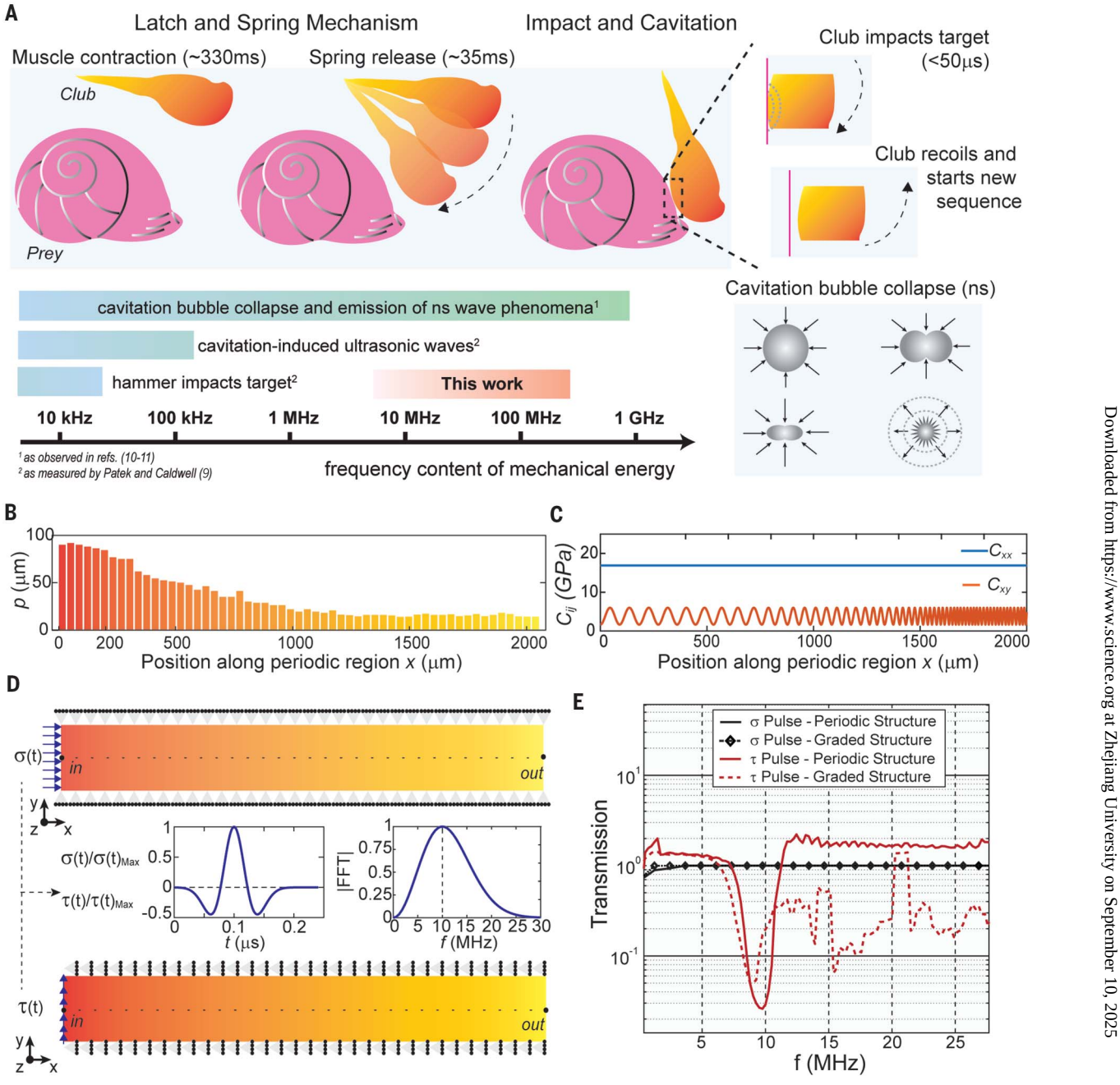

Fig. 4. Role of the mantis shrimp's graded microstructure in impact attenuation. (**A**) Key events in the strike sequence of the smasher mantis shrimp together with relevant timescales and frequency content. (**B**) Spatial modulation of the geometric pitch of the Bouligand microstructure as measured along the median axis of the club. (**C**) Modulation of elastic constants for spatially modulated microstructures with pitch following (B). (**D**) Schematics of FEA models for plane longitudinal and shear wave propagation in response to a Ricker-type pulse (pulse and spectrum are shown in the insets). (**E**) Transmission spectra of single-pitch periodic microstructure and graded microstructure under the applied pulses.

the parallel mode as a Bloch harmonic of the R-wave. The experimental detection of these modes highlights the high-quality periodicity of the structure, akin to a phononic crystal. Additionally, R-wave folding above the bandgap is observed but partially masked by air oscillations. Interestingly, when a simplified model consisting of laminates with isotropic plies exhibiting an oscillating elastic modulus is used, the model also captures the emergence of SSL-wave and R-wave Bloch harmonics [see supplementary text section S4 and (*27*)].

PLU experiments

Thus far, TGS experiments provided insight into the first-order hierarchical features within the periodic region of the mantis shrimp's dactyl club, revealing characteristics associated with the helicoidal laminate structure. At a finer hierarchical level (i.e., at smaller wavelengths), individual elements of the helicoidal laminate, such as chitin fiber bundles embedded in a soft matrix with an interfiber distance of ~1 μm (*17*), become discernible.

Downloaded from https://www.science.org at Zhejiang University on September 10, 2025

Scanning electron microscopy (SEM) images taken from a cracked portion of the club (Fig. 2, D and E) show these details. To explore this finer hierarchy, we used the ultrafast PLU technique, which involves femtosecond pump pulses focused normal to the sample surface, creating a circular spot (~1.25 μm in diameter). The pump pulses generated thermoelastic expansion in the Al layer, launching a broadband SAW pulse that propagated in the *x*-*z* plane of the sample. Time-domain detection was achieved through asynchronous optical sampling (ASOPS) between the pump and probe pulses (see materials and methods section S4) (*28*). The spatial information of the traveling waves is obtained by scanning the pump relative to the probe in a one-dimensional (1D) fashion (Fig. 1E), allowing the generation of space-time diagrams. From these diagrams, SAW dispersion curves are extracted by 2D Fourier transformation. This ASOPS-based PLU setup enables the resolution of wavelengths down to 2.5 μm, with the ability to probe surface modes up to several GHz (*29*). Thus, the technique extends the experimental window to wavelengths approaching the composite-layer characteristic length (e.g., fiber bundle diameter and interfiber distance) and, owing to the point-source geometry, also allows exploration of potential 3D effects that arise from material anisotropy and structure.

Figure 2F presents the dispersion diagram obtained with the PLU technique, highlighting two key observations. First, a primary SAW mode is observed with a phase velocity of 1350 m s^{-1}, closely matching the R-wave identified in TGS experiments (~6% difference). We identified this mode as the R-wave. Unlike the R-wave in TGS, this mode is dispersive, as evidenced by the folding near the end of the accessible wave number range (k ~ 2.1 μm^{-1}). Additionally, a flat branch is observed around ~450 MHz, extending across the entire probed wave number range. A small bandgap (~20 MHz) is identified between the R-wave mode and the flat mode. Notably, the R-wave mode was not detected for wave numbers $k < 1\,\mu m^{-1}$. This can be attributed to two factors: the influence of the pump-related thermal background (low-frequency) near the pump and probe laser beams and the 3D effects inherent to the PLU technique due to point-source generation, which lead to wave attenuation at the observation point. This feature is important not only for interpreting the PLU results but also for gaining insights into the biomechanical function of the club, as discussed in the next section.

We conducted FEM simulations for a microstructure with a pitch of ~11 μm to interpret the PLU results, capturing acoustic wavelengths down to ~2.5 μm. The predicted R-wave mode matches experimental data, with a flat branch near ~425 MHz, though its intensity is overshadowed by the stronger R-wave mode. Zooming into the first two BZs reveals the nondispersive SSL-wave and the dispersive R-wave, which exhibit a broader bandgap (50 to 75 MHz) due to folding. At higher frequencies, two flat branches are predicted: one at 405 MHz and another at 425 MHz. The first flat branch corresponds to the flattening of the R-wave mode observed in experiments, whereas the second flat branch shows qualitative agreement with the experimental flat mode that spans the entire range of probed wave numbers. Although there are slight discrepancies in frequency (likely due to assumed material properties and model geometrical assumptions), the gap between these branches (~20 MHz) is in close agreement with the experimental observations. To further investigate the mode shapes related to these branches, we performed 3D simulations with Bloch-Floquet periodic boundary conditions [see supplementary text section S5 and (*30*)]. These simulations revealed that the flat branch (fig. S6) is predominantly a surface mode, with both horizontal (z) and vertical (y) displacement components, indicative of a zero-group velocity ($\partial\omega/\partial\kappa \approx 0$) mode, where the energy is localized within the structure (no propagation). The detection of these experimental features confirms the phononic characteristics of the mantis shrimp's periodic region and highlights the influence of 3D effects arising from the complex material anisotropy and club structure in this region.

Elastic wave filtering as strategy for impact mitigation

In the preceding sections, we presented an experimental evaluation of the phononic behavior of the mantis shrimp's dactyl club, at the local level within its periodic region, and its interpretation through modeling. We now shift focus to exploring the integrated wave-filtering capabilities of the club's periodic region in the context of the dactyl club's strike. Specifically, we address two key questions: What is the role of the graded Bouligand structure from a phononics perspective and what are the implications of selective filtering of MHz shear waves?

The mantis shrimp's strike involves a series of energy release mechanisms, starting with muscle contraction and energy storage, followed by a latch-like release, and culminating in the club's high-speed impact on the target, accompanied by the generation and collapse of cavitation bubbles (Fig. 4A). Although the impact phase represents less than 0.1% of the total strike sequence duration (*8*), its temporal characteristics are crucial for understanding the role of the discovered phononic mechanisms. The initial contact with the target lasts under 50 μs (*14*) and resembles a pyrotechnic shock, characterized by high-frequency, short-duration, and high-magnitude stress waves consistent with kHz-range vibrations (*23*, *31*). Following this, the collapse of cavitation bubbles violently releases energy over tens of nanoseconds, generating shockwaves in the MHz range (*8*, *32*, *33*), potentially reaching frequencies up to 1 GHz (~ns^{-1}) (*11*). Although both the contact blow and cavitation blow are used by the mantis shrimp to strike its prey, the cavitation blow has only about half the peak force of the initial contact blow but exhibits a much higher frequency spectrum (*9*). Moreover, the hierarchical multilayer structure of the dactyl club, as predicted by FEA, concentrates the highest principal stresses near the impact surface, allowing lower-amplitude, high-frequency stress waves to propagate through the periodic region (*14*). These observations emphasize the importance of high-frequency waves in the shrimp's impact dynamics.

Owing to the rapid dynamics of the strike, experimental measurements of the impact's frequency spectrum have so far been limited to vibrations up to 170 kHz (*9*). However, this upper limit reflects the limitations of the sensing devices rather than the absence of higher-frequency energy transport. In this context, our observations of phononic dispersion, including Bragg bandgaps in the tens of MHz range within the periodic region, align with other shrimp-inspired phononic studies (*34*). These findings suggest that the mantis shrimp uses phononic mechanisms to shield itself from high-frequency transients associated with cavitation-induced shocks during impact (Fig. 4A). Furthermore, they underscore the importance of reevaluating the dynamics of the shrimp's powerful strike using more advanced instrumentation.

To advance this understanding, we evaluated the effectiveness of the mantis shrimp's functionally graded microstructure in mitigating impact under representative conditions. We used a 2D, linear elastic finite element plane-wave model (Fig. 4, B to D) to independently simulate longitudinal and transverse bulk wave propagation across Bouligand microstructures that mimic those of the mantis shrimp. This simplified model was used to isolate the effects of microstructure on bulk wave propagation, which avoided the complexities that arise during a dactyl club strike event, such as underwater fluid-structure interaction, 3D effects, wave propagation across multiple regions, and the curvature of the club's surface. In our simplified 2D strip model, we replicated the geometrically graded structure of the periodic region by incorporating the variation in pitch length observed in dactyl club cross sections (Fig. 4, B and C). Alongside the geometric grading, we accounted for spatially modulated anisotropic elastic properties, varying the components of the stiffness tensor as a function of position, as illustrated in Fig. 4B. To benchmark the graded microstructure,

Downloaded from https://www.science.org at Zhejiang University on September 10, 2025

we compared it against a simpler single-pitch microstructure corresponding to the largest pitch measured in our dactyl club samples (80 μm). This control design not only reflected the location of larger pitches closer to the impact surface but also accounted for their tendency to generate Bragg gaps at lower frequencies. To excite longitudinal and transverse waves, we applied a spatially uniform pulse centered at 10 MHz (Fig. 4D) modeled as a normal pressure [$\sigma(t)$] and a tangential traction [$\tau(t)$], respectively (where t is time). Although detailed modeling of the underwater dynamics of the mantis shrimp's strike is beyond the scope of this study, the effects of the cavitation blow are approximated through the applied stress pulse and material properties validated by surface wave experiments. (For an evaluation of MHz phononic behavior under hydrated conditions, refer to supplementary text section S7). We quantified wave attenuation by comparing the frequency spectrum at the end of the domain (node "out" in Fig. 4D) with that of the applied pulse (node "in" in Fig. 4D). Further details of the modeling approach are provided in the materials and methods.

The frequency spectra of transmitted normal and shear stress components, for both single-pitch and graded models, are displayed in Fig. 4E. For longitudinal stress waves, the input and output stress spectrograms overlap, indicating no notable filtering. This is expected, because the variation of the material stiffness in the x direction is invariant of position, that is, the medium is uniform for longitudinal waves propagating in the x direction. By contrast, for shear waves, the spectrograms reveal a pronounced influence of the microstructural arrangement. In the single-pitch microstructure, a frequency dip centered around 8 MHz aligns with the bandgap predicted from the dispersion diagrams (see supplementary text section S6). For the graded microstructure, a much broader gap emerges, spanning most of the frequency range of the applied pulse. This highlights the structural gradient's ability to affect a wider frequency range. Signal energy calculations show that 100% of the incoming pressure pulse is transmitted, whereas only 66 and 43% of the shear pulse energy is transmitted through the single-pitch periodic and graded-pitch structures, respectively.

Beyond the linear plane wave model, which emphasizes the interaction between microstructure and high-frequency waves in shielding against nanosecond-scale shockwaves, we note that real-world impacts may act as point sources. In such cases, bulk elastic waves could diffract in three dimensions, further broadening the frequency range of filtering. Furthermore, if bulk waves are not plane waves propagating strictly along the periodic region, even longitudinal waves could become sensitive to the periodic variation in elastic properties. Consequently, most wave energy and frequency content would be filtered, with only a fraction propagating through (primarily polarized and traveling along the x-direction).

Selective filtering of shear waves, by Bouligand-like spatially modulated structures, hints at the potentially detrimental effects of these waves to the dactyl club's functionality. Extensive experimental and computational studies on behind-armor blunt trauma (nonpenetrating impacts) have demonstrated that gross motions induced by shear waves are critical contributors to damage in organs and tissues, leading to lacerations, contusions, interfacial disruptions, and fractures (*35*–*37*). Shear waves are also linked to traumatic brain injuries, such as diffuse axonal injury, through mechanisms such as shear wave focusing and shear shock-wave generation with high-frequency harmonic components (*38*, *39*). Given the precise neural control required for the mantis shrimp's striking motion (*40*), protecting nerve fibers is essential, because it ensures the structural integrity of the club's tissue and the organic membranes within, particularly during high-strain-rate events and successive molting cycles (*41*, *42*). Similarly, in synthetic materials, transverse (shear) waves have been shown to cause delamination and interlayer cracking in impact-resistant composites, compromising their structural integrity and dynamic load resistance (*43*, *44*). The mantis shrimp's design, which selectively shields against the highest frequencies rather than the entire spectrum, reflects an advanced strategy that recognizes that strain rate can be as damaging as, or more damaging than, load magnitude, a phenomenon observed in studies on the effects of ultrasound (*35*, *42*). This selective filtering also relates to the overall size limitation of the periodic region within the dactyl club, given that filtering lower frequencies would require larger pitches. Furthermore, the periodic region provides additional advantages, including enhanced toughness attributed to the Bouligand architecture (*45*, *46*). This architectural motif offers dual benefits: high-frequency phononic filtering and mechanical toughening. Interestingly, these phenomena may not be independent but rather interdependent, with phononic mechanisms potentially enhancing extrinsic toughening by facilitating stable crack growth and mitigating catastrophic failure (*47*, *48*).

Discussion and conclusions

The mantis shrimp has long been regarded as a paragon of biological engineering owing to its notable impact-related properties. More recently, numerical analyses have suggested that the helicoidal fiber arrangement in the periodic region of the dactyl club gives rise to phononic shear wave bandgaps, complementing the suite of defensive mechanisms of the mantis shrimp.

By combining nanosecond and picosecond laser ultrasonic techniques with modeling, we have presented experimental evidence of phononic behavior facilitated by the Bouligand microstructure of the mantis shrimp. The phononic nature of the periodic region of the dactyl club was revealed through the observation of Bloch harmonics, dispersive surface modes, flat modes, and phononic bandgaps. These observations arise from the interactions of waves with the hierarchical architecture of the dactyl club, as shown by transient wave propagation simulations. Using dynamic finite element models, we assessed the role of the graded Bouligand arrangement in impact mitigation through wave-filtering mechanisms and compared it with simpler microstructural configurations.

We conclude that the graded Bouligand arrangement in the mantis shrimp selectively filters shear waves generated by nanosecond-scale cavitation bubble collapse over an extended range in the lower MHz regime. This characteristic, which stems from the distinctive material and geometric properties of the periodic region, suggests an evolutionary advantage in shielding soft tissues from harmful high-frequency shear waves, which are particularly detrimental to soft tissues and neural synapses.

In the broader context of natural phononic structures, our measurements and analyses extend the known range of functional phononic behavior into the MHz regime, providing evidence of phononic Bragg scattering mechanisms (akin to those seen in phononic crystals), rather than local resonance, as a biological functionality. Additionally, this work highlights nature's ability to engineer a high-quality ultrasonic chirped phononic crystal, exhibiting Bloch harmonics, with a level of sophistication that would typically require advanced micro- and nanomanufacturing techniques. Furthermore, the discovery of flat bands extending into the hundreds of MHz suggests the potential for spatial energy localization, which can be dissipated locally with minimal damping, offering further insights into how these natural structures may mitigate high-frequency energy.

Downloaded from https://www.science.org at Zhejiang University on September 10, 2025

REFERENCES AND NOTES

1. P.-Y. Chen, J. McKittrick, M. A. Meyers, *Prog. Mater. Sci.* **57**, 1492–1704 (2012).
2. F. Barthelat, H. Tang, P. D. Zavattieri, C.-M. Li, H. D. Espinosa, *J. Mech. Phys. Solids* **55**, 306–337 (2007).
3. H. D. Espinosa *et al.*, *Nat. Commun.* **2**, 173 (2011).
4. H. D. Espinosa *et al.*, *Matter* **1**, 1246–1261 (2019).
5. M. Asgari, N. A. Alderete, Z. Lin, R. Benavides, H. D. Espinosa, *Acta Biomater.* **122**, 236–248 (2020).
6. M. J. Chon *et al.*, *J. Mech. Behav. Biomed. Mater.* **76**, 30–37 (2017).
7. A. Sakes *et al.*, *PLOS ONE* **11**, e0158277 (2016).
8. S. N. Patek, *Integr. Comp. Biol.* **59**, 1573–1585 (2019).

9. S. N. Patek, R. L. Caldwell, *J. Exp. Biol.* **208**, 3655–3664 (2005).
10. D. Lohse, B. Schmitz, M. Versluis, *Nature* **413**, 477–478 (2001).
11. J. Holzfuss, M. Rüggeberg, A. Billo, *Phys. Rev. Lett.* **81**, 5434–5437 (1998).
12. R. Pecha, B. Gompf, *Phys. Rev. Lett.* **84**, 1328–1330 (2000).
13. J. R. Shorter, O. Rueppell, *Insectes Soc.* **59**, 1–10 (2012).
14. J. C. Weaver *et al*., *Science* **336**, 1275–1280 (2012).
15. W. Huang *et al*., *Nat. Mater.* **19**, 1236–1243 (2020).
16. N. A. Yaraghi *et al*., *Adv. Mater.* **28**, 6835–6844 (2016).
17. L. K. Grunenfelder *et al*., *Acta Biomater.* **10**, 3997–4008 (2014).
18. N. Guarín-Zapata, J. Gomez, N. Yaraghi, D. Kisailus, P. D. Zavattieri, *Acta Biomater.* **23**, 11–20 (2015).
19. F. Bosia *et al*., *Matter* **5**, 3311–3340 (2022).
20. P. Vukusic, J. R. Sambles, *Nature* **424**, 852–855 (2003).
21. T. R. Neil, Z. Shen, D. Robert, B. W. Drinkwater, M. W. Holderied, *Proc. Natl. Acad. Sci. U.S.A.* **117**, 31134–31141 (2020).
22. S. K. Yang, V. V. Varadan, A. Lakhtakia, V. K. Varadan, *J. Phys. D Appl. Phys.* **24**, 1601–1608 (1991).
23. H. Le Ferrand, *Compos. Struct.* **224**, 111105 (2019).
24. J. A. Rogers, A. A. Maznev, M. J. Banet, K. A. Nelson, *Annu. Rev. Mater. Sci.* **30**, 117–157 (2000).
25. A. A. Maznev, K. A. Nelson, J. A. Rogers, *Opt. Lett.* **23**, 1319–1321 (1998).
26. W. P. Mason, R. N. Thurston, *Physical Acoustics: Principles and Methods* (Academic Press, 1972).
27. T. C. Lim, P. Cheang, F. Scarpa, *Phys. Status Solidi, B Basic Res.* **251**, 388–396 (2014).
28. A. Abbas *et al*., *Opt. Express* **22**, 7831–7843 (2014).
29. Q. Xie *et al*., *Nat. Commun.* **10**, 2228 (2019).
30. R. S. Westafer, thesis, Georgia Institute of Technology (2011).
31. J. R. Lee, C. C. Chia, C. W. Kong, *Measurement* **45**, 631–642 (2012).
32. C. E. Brennen, *Cavitation and Bubble Dynamics*, Oxford Engineering Science Series (Oxford Univ. Press, 1995).
33. Y. Tomita, A. Shima, *J. Fluid Mech.* **169**, 535–564 (1986).
34. R. P. Behera, H. Le Ferrand, *Matter* **4**, 2831–2849 (2021).
35. L. Cannon, *J. R. Army Med. Corps* **147**, 87–96 (2001).
36. Institute of Medicine, *Long-term Effects of Blast Exposures*, vol. 9 of *Gulf War and Health* (National Academies Press, 2014).
37. G. J. Cooper, D. E. Taylor, *J. R. Army Med. Corps* **135**, 58–67 (1989).
38. S. Chandrasekaran *et al*., *J. Biomech.* **166**, 112021 (2024).
39. B. Giammarinaro, D. Espíndola, F. Coulouvrat, G. Pinton, *Phys. Rev. Appl.* **9**, 014011 (2018).
40. M. Burrows, *J. Comp. Physiol. A Neuroethol. Sens. Neural Behav. Physiol.* **62**, 361–381 (1969).
41. S. Amini *et al*., *Proc. Natl. Acad. Sci. U.S.A.* **116**, 8685–8692 (2019).
42. Z. Izadifar, P. Babyn, D. Chapman, *Ultrasound Med. Biol.* **43**, 1085–1104 (2017).
43. H. D. Espinosa, S. Dwivedi, H. C. Lu, *Comput. Methods Appl. Math.* **183**, 259–290 (2000).
44. Y. B. Gao, L. T. Shi, T. Lu, W. B. Xie, X. M. Cai, *Eng. Fract. Mech.* **295**, 109797 (2024).
45. N. Suksangpanya, N. A. Yaraghi, D. Kisailus, P. Zavattieri, *J. Mech. Behav. Biomed. Mater.* **76**, 38–57 (2017).
46. A. Zaheri *et al*., *Adv. Funct. Mater.* **28**, 1803073 (2018).
47. F. Atrash, A. Hashibon, P. Gumbsch, D. Sherman, *Phys. Rev. Lett.* **106**, 085502 (2011).
48. B. Davies *et al*., *Sci. Rep.* **4**, 7538 (2014).

ACKNOWLEDGMENTS

We thank R. Fulcrand for assistance with SEM image acquisition. **Funding:** H.D.E. acknowledges financial support from the Air Force Office of Scientific Research (AFOSR) through award no. FA9550-20-1-0258, the Office of Naval Research (award no. N000142212133), and the National Science Foundation (award no. CMMI-1953806). M.A.G. acknowledges financial support from the Institut Lumière Matière (ILM) and Fédération de Recherche André-Marie Ampère (FRAMA) through start-up funds. **Author contributions:** Conceptualization: N.A.A., M.A.G., H.D.E.; Methodology: N.A.A., S.R., M.A.G., H.D.E.; Resources: M.A., H.D.E.; Investigation: N.A.A., S.S., S.R., M.A.G., H.D.E.; Visualization: N.A.A., M.A.G., H.D.E.; Funding acquisition: M.A.G., H.D.E.; Project administration: H.D.E.; Supervision: H.D.E.; Writing – original draft: N.A.A., M.A.G., H.D.E.; Writing – review & editing: S.R., H.D.E. **Competing interests:** The authors declare that they have no competing interests. **Data and materials availability:** All data are available in the main text or the supplementary materials. **License information:** Copyright © 2025 the authors, some rights reserved; exclusive licensee American Association for the Advancement of Science. No claim to original US government works. https://www.science.org/about/science-licenses-journal-article-reuse

SUPPLEMENTARY MATERIALS

science.org/doi/10.1126/science.adq7100
Materials and Methods
Supplementary Text
Figs. S1 to S10
Table S1
References

Submitted 27 May 2024; accepted 9 December 2024
10.1126/science.adq7100

Downloaded from https://www.science.org at Zhejiang University on September 10, 2025